MOX-Report No. 56/2016

A computational fluid-structure interaction analysis of coronary Y-grafts

Guerciotti, B.; Vergara, C.; Ippolito, S.; Quarteroni, A.; Antona, C.; Scrofani, R.

MOX, Dipartimento di Matematica
Politecnico di Milano, Via Bonardi 9 - 20133 Milano (Italy)

mox-dmat@polimi.it http://mox.polimi.it

A computational fluid-structure interaction analysis of coronary Y-grafts

Bruno Guerciotti[1,*] Christian Vergara[1] Sonia Ippolito[2]
Alfio Quarteroni[3] Carlo Antona[4] Roberto Scrofani[4]

[1] MOX - Department of Mathematics, Politecnico di Milano, Piazza Leonardo da Vinci 32, 20133 Milano, Italy, (*) bruno.guerciotti@polimi.it
[2] Radiology Unit, Ospedale L. Sacco, via G.B. Grassi 74, 20157 Milano, Italy
[3] SB MATHICSE CMCS, EPFL, av. Piccard, Bat. MA, Sec. B2-C2, Station 8, CH-1015 Lausanne, Switzerland
[4] Cardiosurgery Unit, Ospedale L. Sacco, via G.B. Grassi 74, 20157 Milano, Italy

Abstract

Coronary artery disease is one of the leading causes of death worldwide. The stenotic coronary vessels are generally treated with coronary artery bypass grafts (CABG), which can be either arterial (internal mammary artery, radial artery) or venous (saphenous vein). However, the different mechanical properties of the graft can influence the outcome of the procedure in terms of risk of restenosis and subsequent graft failure. In this paper, we perform a computational fluid-structure interaction (FSI) analysis of patient-specific multiple CABGs (Y-grafts) with the aim of better understanding the influence of the choice of bypass (arterial vs venous) on the risk of graft failure. Our results show that the use of a venous bypass results in a more disturbed flow field at the anastomosis and in higher stresses in the vessel wall with respect to the arterial one. This could explain the better long-term patency of the arterial bypasses experienced in the clinical practice.

Keywords: CABG; intimal hyperplasia; restenosis; FSI; non-Newtonian rheology

1 Introduction

Coronary artery bypass graft (CABG) surgery, the standard procedure to treat advanced coronary artery disease, consists in bypassing a blocked portion of a coronary artery in order to restore the proper blood flow to the heart. The bypass used for the procedure is typically autologous, i.e., harvested from the patient's own body. In case of patients with isolated left anterior descending (LAD) coronary artery disease, the recommended treatment is the use of the left internal mammary artery (LIMA) bypass, due to its excellent long-term patency rate [22]. For patients with multivessel coronary disease, together with LIMA, other types of grafts are used to bypass the remaining coronary occlusions [36]. In particular, arterial or venous grafts may be used either as a conventional

free (i.e., connected proximally to the aorta and distally to the diseased coronary vessel) or *composite* (i.e., connected proximally to the first graft, usually the LIMA, and distally to the diseased coronary artery) bypasses. In the latter case, two of the most common choices for the second graft are the radial artery (RA) and the saphenous vein (SV), which are typically attached with a Y anastomosis to the LIMA graft to form a *composite Y-graft* [9, 42]. RA and SV grafts have both advantages and disadvantages (see [42] for a review) and today there is still controversial evidence regarding the best choice. As a matter of fact, several clinical trials have demonstrated better long-term patency rates for arterial conduits (see e.g. [3, 11, 14]), however SV remains one of the most widely used graft because of its accessibility, sufficient length, ease of use, and in those cases where the radial artery cannot be used (e.g. when the Allen's test shows inadequate collateral hand perfusion or in presence of a non-severe coronary artery stenosis) [2, 5, 58].

The main factor affecting graft patency is the development of intimal hyperplasia (IH) at the anastomosis between the graft and the coronary artery. IH is the progressive intimal thickening due to abnormal proliferation of smooth muscle cells in the tunica intima of the vessel wall, which results in the reduction of the lumen of the graft and may eventually lead to restenosis and graft failure [35, 38, 40]. Although the underlying mechanisms of IH development have not been completely elucidated yet, suggested hypotheses are the presence of hemodynamic disturbances (e.g., stagnation and recirculation regions) and localized stress concentrations in the graft wall, especially in the region of the anastomosis [7, 32, 48, 53]. In particular, extensive IH formation typically occurs when a compliance mismatch between the graft and the host coronary artery is present.

Many computational studies have addressed the problem of finding a possible correlation between hemodynamics in CABGs and IH development, see [46] for a review of recent numerical investigations. Most of them focused on the quantification of hemodynamic parameters to explore the theory of IH development due to the disturbed fluid-dynamics (see e.g. [17, 60]). Only a few authors have attempted to study the influence of mechanical factors like internal wall stresses on HI. In these studies, accurate models of the vessel wall mechanics were considered. For instance, some authors prescribed a given internal pressure to surrogate the blood dynamics [6].

Within this context, the fluid-structure interaction (FSI) between blood and the vessel walls should provide a better quantification of the internal wall stresses and at the same time would allow to assess also the fluid-dynamic factors. However, no numerical FSI simulations in patient-specific CABG geometries have been made so far. Furthermore, despite the ever-increasing clinical interest in the use of composite Y-grafts and the search for the best graft to be used (RA vs SV), no numerical investigations have been made to compare the effects of the graft choice on the resulting fluid-dynamic and mechanical factors that may contribute to the failure of the graft.

The purpose of this work is to investigate the possible causes of graft failure in patient-specific multiple Y-CABGs, with particular attention to the fluid-dynamics and wall mechanics resulting from different choices (arterial vs venous). With this aim, we perform a computational FSI analysis in three patients with multivessel coronary disease and treated with a Y-graft. In particular, we characterize different grafts by changing their mechanical properties (Young's modulus) and geometric characteristics (diameter). Since the risk of graft fail-

	Coronary arteries	Stenoses	Bypass grafts
P1	LMCA LAD LCx	LAD LCx	LIMA-to-LAD RA Y-graft on LIMA-LCx
P2	LMCA LAD LCx-OM	LAD OM	LIMA-to-LAD RA Y-graft on LIMA-OM
P3	LMCA LAD-diag LCx	LAD diag	LIMA-to-LAD SV Y-graft on LIMA-diag

Table 1: Recontructed coronary vessels and bypass grafts for each patient. LMCA = left main coronary artery; LCx = left circumflex artery; OM = obtuse marginal artery; diag = diagonal branch of LAD.

ure is related to the degree of coronary stenosis [8, 37], for each case we consider three possible degrees (50%, 70%, 90%) to assess the fluid-mechanic and mechanical factors in relation to the severity of the stenosis.

2 Materials and Methods

2.1 Patients dataset

In this study, we consider three patients (P1, P2 and P3 in the following) with severe multivessel coronary artery disease who underwent off-pump CABG surgery with a composite Y-graft. In particular, these patients featured two stenoses, one in LAD and another one in a second coronary vessel, see Table 1 for details. In what follows, we refer to these as *LAD stenosis* and *second stenosis*. The patients were treated with a LIMA bypass to restore LAD perfusion and with a second graft (radial artery for P1 and P2 and saphenous vein for P3), proximally attached to LIMA, to bypass the second stenosis, see Figure 1, top.

The follow-up study, based on three-dimensional Contrast Enhanced Computed Tomography (3D-CE-CT), was performed with a Philips Brilliance CT 64-slice system with the following main acquisition parameters: slice thickness $0.67\,mm$, slice spacing $0.33\,mm$, reconstruction matrix 512×512 pixels, final resolution $0.45\,mm \times 0.45\,mm \times 0.33\,mm$.

2.2 Computational domains and mesh generation

The reconstruction of the 3D surface models representing the interface between blood and the vessel walls was performed with a level-set segmentation technique developed in the software VMTK (http://www.vmtk.org) starting from the CT images of the three patients. We report in Table 1 the details of the reconstructed coronary vessels and bypasses and in Figure 1, top, the resulting reconstructed 3D geometries (in what follows, we refer to these as *original geometries*).

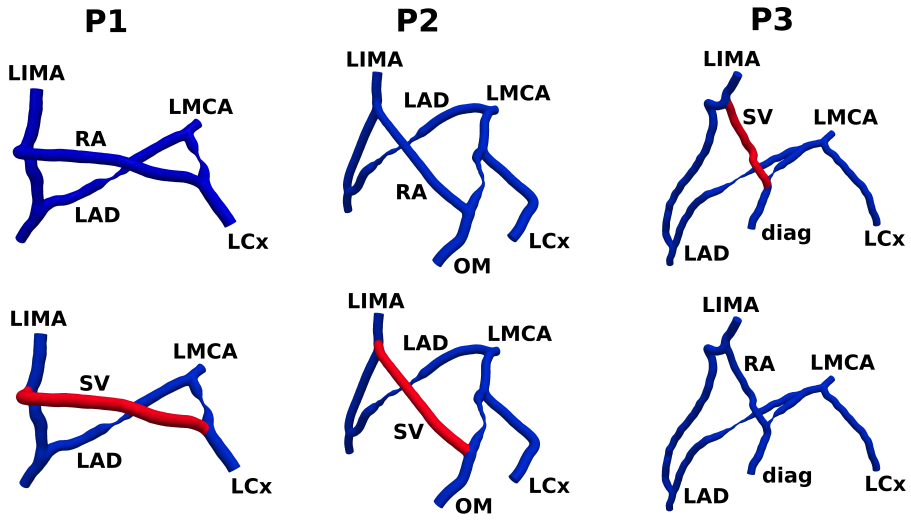

Figure 1: Top: Reconstructed 3D original geometries for patients P1 (left), P2 (middle) and P3 (right). Bottom: Corresponding modified geometries where RA was substituted by SV in P1 and P2, whereas SV was substituted by RA in P3. Young's modulus $E = E_A = 1 \times 10^5\, Pa$ for the arteries (in blue) and $E = E_V = 1 \times 10^6\, Pa$ for the venous graft (in red).

The main aim of this work is to compare the mechanical answers of two different Y-grafts commonly implanted to bypass the second stenosis. In particular, we consider the radial artery (RA) and the saphenous vein (SV), ideally implanted in the same patient in order to discard other possible sources of difference. To this aim, we characterized the two grafts as follows:

1) by using different Y-grafts diameters (SV is bigger than RA);

2) by using different values of Young's modulus (SV graft is stiffer than RA graft, see Discussion).

In view of the first point, for each patient we created a second *modified geometry* obtained by virtually changing the Y-graft diameter. In particular, both for P1 and P2, the SV Y-graft modified geometry was characterized by a diameter of $3.5\, mm$ [12] (original RA bypass diameters of about $2.4\, mm$ and $2.7\, mm$, respectively), whereas for P3 the RA Y-graft modified geometry was characterized by a diameter of $2.5\, mm$ [12] (original SV bypass diameter of about $3.2\, mm$).

As for point 2 above, in the numerical simulations we used $E = E_A = 1 \times 10^5\, Pa$ for RA [30] and $E = E_V = 1 \times 10^6\, Pa$ [57]. For the remaining (arterial) part of the geometries (both original and modified), we set $E = 1 \times 10^5\, Pa$. See Figure 1.

For each of the six considered cases (RA and SV Y-grafts for each of the three patients), we virtually varied the degree of the second stenosis (located in LCx, OM and diag for patients P1, P2 and P3, respectively, see Table 1), maintaining the LAD stenosis degree to its original value of 90%. In particular, we considered

three virtual scenarios characterized by 50%, 70%, and 90% stenosis degree. This was obtained by means of the technique proposed and reported in [20].

In view of the numerical simulations, for each of the eighteen geometries (three second stenosis degrees for each of the six cases), we created the volumetric meshes of tetrahedra for the fluid domain. Local mesh refinements were performed at the level of the stenoses, proportional to the degree of the stenosis. The resulting number of tetrahedra were about 350k, 650k, and 660k for P1, P2 and P3, respectively, for both the original and modified geometries. Then, we created the meshes for the solid domain by extruding outward the fluid mesh and selecting a total wall thickness of 0.5mm, which is a reasonable value for both the coronary arteries [61] and the grafts [10]. The resulting number of tetrahedra for the solid meshes were about 250k, 460k and 500k for P1, P2 and P3, respectively, for both the original and modified geometries. We report in Figure 2 some details of the fluid and solid meshes of P1.

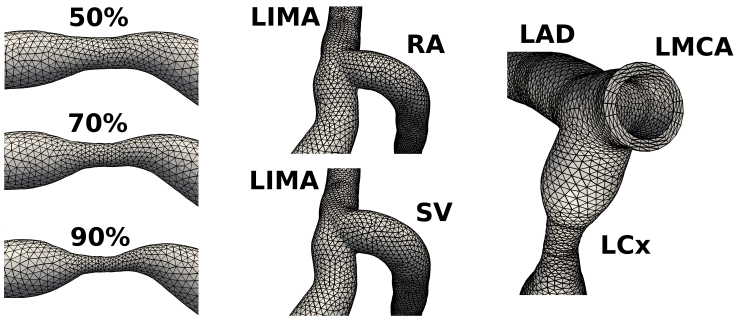

Figure 2: Details of the fluid and solid meshes of P1. Left: different coronary stenosis degrees (LCx) of the fluid domain for the RA case. Middle: different fluid meshes for the RA and SV Y-graft cases. Right: solid mesh at the LMCA bifurcation for the RA case.

2.3 Governing equations and boundary conditions

Referring to Figure 3, let Ω_f and Ω_s be the current fluid and structure domains, respectively. In the first one, the Navier-Stokes equations for an incompressible, homogeneous, non-Newtonian fluid, written in the *Arbitrary Lagrangian-Eulerian* (ALE) configuration [25, 15], are solved to model the blood flow, whereas in the second one we consider the linear infinitesimal elasticity (Hooke's law) to model the wall mechanics.

For any function w defined in the current fluid (solid) configuration, we denote by $\widehat{w}$ its counterpart in the reference domain $\widehat{\Omega}_f$ ($\widehat{\Omega}_s$). The common FS interface is denoted by Σ. Then, the FSI problem reads as follows:

Find, at each time $t \in (0, T]$, fluid velocity $\boldsymbol{v}_f$, pressure p_f, structure displace-

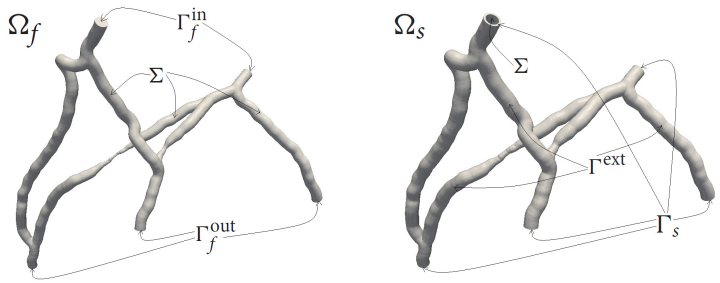

Figure 3: Computational domains. Fluid domain on the left, structure domain on the right.

ment $\boldsymbol{d}_s$, and fluid domain displacement $\boldsymbol{d}_m$, such that

$$\rho_f \frac{\delta \boldsymbol{v}_f}{dt} + \rho_f((\boldsymbol{v}_f - \boldsymbol{v}_m)\cdot\nabla)\boldsymbol{v}_f - \nabla\cdot(2\mu(\boldsymbol{v}_f)\boldsymbol{D}(\boldsymbol{v}_f)) + \nabla p = \boldsymbol{0} \quad \text{in } \Omega_f, \tag{1a}$$

$$\nabla\cdot\boldsymbol{v}_f = 0 \quad \text{in } \Omega_f, \tag{1b}$$

$$\mu(\boldsymbol{x},t) = \mu_\infty + (\mu_0 - \mu_\infty)\left(1 + (\lambda\dot{\gamma}(\boldsymbol{x},t)^a\right)^{\frac{n-1}{a}} \quad \text{in } \Omega_f, \tag{1c}$$

$$\boldsymbol{v}_f = \boldsymbol{g} \quad \text{at } \Gamma_f^{in}, \tag{1d}$$

$$\frac{1}{|\Gamma_f^{out}|}\int_{\Gamma_f^{out}} (\boldsymbol{T}_f\,\boldsymbol{n})\cdot\boldsymbol{n}\,d\sigma - R_e\int_{\Gamma_f^{out}} \boldsymbol{v}_f\cdot\boldsymbol{n}\,d\sigma = 0 \quad \text{at } \Gamma_f^{out}, \tag{1e}$$

$$\boldsymbol{v}_f = \frac{\partial \boldsymbol{d}_s}{\partial t} \quad \text{at } \Sigma, \tag{1f}$$

$$\boldsymbol{T}_s(\boldsymbol{d}_s)\,\boldsymbol{n} - \boldsymbol{T}_f(\boldsymbol{v}_f, p_f)\,\boldsymbol{n} = \boldsymbol{0} \quad \text{at } \Sigma, \tag{1g}$$

$$\rho_s \frac{\partial^2 \widehat{\boldsymbol{d}}_s}{\partial t^2} - \nabla\cdot\widehat{\boldsymbol{T}}_s(\widehat{\boldsymbol{d}}_s) = \boldsymbol{0} \quad \text{in } \widehat{\Omega}_s, \tag{1h}$$

$$\widehat{\boldsymbol{d}}_s = \boldsymbol{0} \quad \text{at } \widehat{\Gamma}_s, \tag{1i}$$

$$\alpha_e\widehat{\boldsymbol{d}}_s + \widehat{\boldsymbol{T}}_s(\widehat{\boldsymbol{d}}_s)\,\widehat{\boldsymbol{n}} = \boldsymbol{0}, \quad \text{at } \widehat{\Gamma}^{ext}, \tag{1j}$$

$$-\triangle\widehat{\boldsymbol{d}}_m = \boldsymbol{0} \quad \text{in } \widehat{\Omega}_f, \tag{1k}$$

$$\widehat{\boldsymbol{d}}_m = \widehat{\boldsymbol{d}}_s \quad \text{at } \widehat{\Sigma}, \tag{1l}$$

where $\widehat{\boldsymbol{v}}_m = \frac{\partial\widehat{\boldsymbol{d}}_m}{\partial t}$ is the fluid mesh velocity.

In the previous coupled problem, (1a)-(1b) represent the fluid problem, (1h) the structure problem, and (1k) the harmonic extension for the computation of the fluid domain. Moreover, $\rho_f = 1.06\,g/cm^3$ and $\rho_s = 1.1\,g/cm^3$ are the fluid and structure densities; $\boldsymbol{n}$ is the unit normal exiting from the fluid domain, $\frac{\delta}{dt} = \frac{\partial}{\partial t} + (\boldsymbol{v}_f\cdot\nabla)$ the ALE derivative, $\boldsymbol{D}(\boldsymbol{w}) = \frac{1}{2}\left(\nabla\boldsymbol{w} + (\nabla\boldsymbol{w})^T\right)$, $\widehat{\boldsymbol{T}}_s(\widehat{\boldsymbol{d}}_s) = 2\lambda_1\boldsymbol{D}(\widehat{\boldsymbol{d}}_s) + \lambda_2\boldsymbol{I}\nabla\cdot\widehat{\boldsymbol{d}}_s$ the first Piola-Kirchhoff tensor, and $\boldsymbol{T}_s(\boldsymbol{d}_s)$ the Cauchy stress tensor of the solid; $\lambda_1 = \frac{E}{2(1+\nu)}$ and $\lambda_2 = \frac{E\nu}{(1+\nu)(1-2\nu)}$ are the two Lamé constants, with E Young's modulus (see Sect. 2.2) and $\nu = 0.49$ Poisson's ratio. For the non-Newtonian rheology of blood, we choose the Carreau-Yasuda model (1c) [13, 55], with $\lambda = 1.902s$, $n = 0.22$, $a = 1.25$, $\mu_0 = 0.56\,P$, $\mu_\infty = 0.0345\,P$ (μ_∞ represents blood viscosity at "infinite" shear rate, i.e., the viscosity value generally used in case of Newtonian assumption) and the shear rate given by $\dot{\gamma}(\boldsymbol{v}_f) = 2\sqrt{D_{II}}$, where D_{II} denotes the second invariant of the rate of deformation tensor $\boldsymbol{D}(\boldsymbol{v}_f)$. Function $\boldsymbol{g}$ is a parabolic profile used to enforce the

Dirichlet conditions (1d) at the fluid inlets, where the corresponding flow rate waveforms $Q(t) = \int_{\Gamma_f^{in}} \boldsymbol{g}(t) \cdot \boldsymbol{n}$, obtained by the procedure reported in [20] and based on an extended Murray's law for stenotic vessels, are reported in Figure 4. We notice that at LMCA the flow rate is assumed to be independent of the degree of stenosis, as suggested by physiological evidences [28], whereas at LIMA it adapts in order to compensate for the change of flow corresponding to the different stenosis degrees considered at the coronary vessel bypassed by the Y-graft. R_e is the resistance used to enforce the absorbing boundary conditions (1e) at the fluid outlets, see [45, 44] for its computation. For the structure, at the artificial section Γ_s we impose null displacements (1i), whereas at the lateral surface Γ^{ext} we prescribe the Robin condition (1j) assuming an elastic behavior of the surrounding tissue, represented by the myocardium on the side where the coronaries lie and by the pericardium on the opposite side. Here, we consider a unique value of the elastic parameter $\alpha_e = 3 \cdot 10^7\, Pa/m$ as representative of the whole surrounding tissue [39].

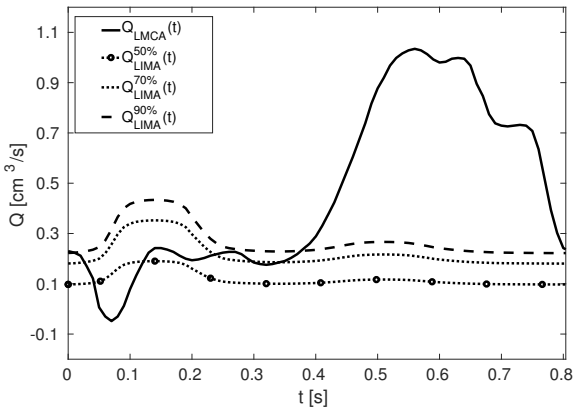

Figure 4: Flow rate waveforms prescribed at the fluid inlets.

At the FS interface, we enforce the matching conditions, which state the continuity of velocities (1f), tractions (1g), and displacements (1l).

Finally, we observe that problem (1) has to be endowed with suitable initial conditions and that $T = 0.8\, s$ is the period of a heartbeat.

For the time discretization of problem (1), we consider a backward Euler method with a semi-implicit treatment of the convective [49] and diffusive [20] terms (the latter one being non-linear because of the non-Newtonian assumption) for the fluid problem and the midpoint/Newmark scheme for the structure one [44]. For the numerical solution of the corresponding linearized FSI problem, we use at each time step the *Robin-Robin* (RR) partitioned scheme [4, 18, 19], with an explicit treatment of the geometric coupling condition (1l) [16]. At each iteration, for the fluid problem we consider P1-bubble/P1 Finite Elements (FE), whereas for the structure P1 FE.

The numerical simulations are obtained using the FE library *LifeV* (`www.lifev.org`).

2.4 Quantities of interest

As indicator of disturbed fluid-dynamics (e.g., presence of recirculation and stagnation regions), we analyze the *Relative Residence Time* (RRT), which is considered as a robust and single metric of low and/or oscillatory Wall Shear Stress (WSS) [33]. RRT is a function of space defined as

$$RRT(\boldsymbol{x}) = \frac{1}{(1 - 2OSI(\boldsymbol{x}))TAWSS(\boldsymbol{x})}, \tag{2}$$

where OSI is the oscillatory shear index

$$OSI(\boldsymbol{x}) = \frac{1}{2}\left(1 - \frac{\left\|\int_0^T \boldsymbol{\tau}_w(\boldsymbol{x}, t)dt\right\|}{\int_0^T \|\boldsymbol{\tau}_w(\boldsymbol{x}, t)\|\, dt}\right)$$

and $TAWSS$ is the time-averaged WSS

$$TAWSS(\boldsymbol{x}) = \frac{1}{T}\int_0^T \|\boldsymbol{\tau}_w(\boldsymbol{x}, t)\|\, dt,$$

with $\boldsymbol{\tau}_w = \boldsymbol{t} - (\boldsymbol{t}\cdot\boldsymbol{n})\boldsymbol{n}$ the wall shear stress vector and $\boldsymbol{t} = 2\mu(\boldsymbol{v}_f)\boldsymbol{D}(\boldsymbol{v}_f)\boldsymbol{n}$ the fluid traction vector acting on the lumen boundary.

As for the analysis of the wall mechanics, we consider the Von Mises (VM) stresses as representative of the complex internal stress state in the vessel wall [31]. VM stresses are defined as

$$T_{VM}(\mathbf{x}, t) = \sqrt{\frac{(T_{11} - T_{22})^2 + (T_{22} - T_{33})^2 + (T_{33} - T_{11})^2 + 6(T_{12}^2 + T_{23}^2 + T_{32}^2)}{2}}, \tag{3}$$

where T_{ij} are the components of the Cauchy stress tensor $\boldsymbol{T}_s$.

3 Results

For each patient and for each stenosis degree, we report in Figure 5 the peak diastolic ($t = 0.56s$) velocity field for the RA graft case. In particular, we plot the streamlines color-coded with the velocity magnitude in a portion of the fluid domain comprising the anastomosis related to the second stenosis and the two stenoses. We do not report here the results corresponding to the SV graft cases because they are very similar. From this figure, we observe a more disturbed fluid-dynamics at the anastomosis of interest for the 50% and 70% degree cases, characterized by swirling patterns typical of recirculation and stagnation regions. We also notice that, for P1 and P2, retrograde flow is present in the RA graft for the 50% and 70% cases.

In order to investigate more in detail the presence of recirculation and stagnation regions at the anastomosis, which is the region where the development of intimal hyperplasia may occur, we report in Figure 6 the RRT distribution (computed with (2)) for each patient and for each stenosis degree, both for RA and SV grafts, in a region of interest around the anastomosis. We notice that RRT values are higher in the cases with lower stenosis degrees for all the three patients and both grafts. Furthermore, RRT values are slightly higher in the

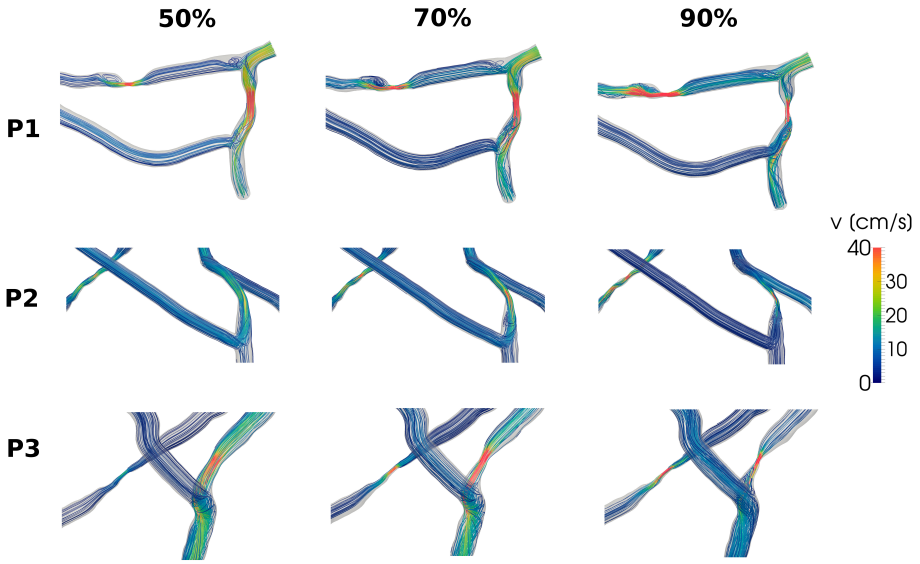

Figure 5: Peak diastolic velocity streamlines (color-coded with velocity magnitude) for P1, P2, and P3 for different second stenosis degrees; in each figure, LAD stenosis is at the left, whereas the second stenosis is at the right; the anastomosis of interest is at the bottom-right. RA graft cases are shown.

Table 2: Averaged-in-space RRT values (in Pa^{-1}) for each patient and stenosis degree, both for RA and SV grafts.

		50%	70%	90%
P1	RA	18.2	4.6	2.9
	SV	26.5	5.9	3.5
P2	RA	22.3	11.9	2.4
	SV	27.5	13.4	4.1
P3	RA	17.1	3.9	3.6
	SV	20.1	5.8	5.7

SV grafts. This general trend is also confirmed by the averaged-in-space RRT values computed in the same regions of interest of Figure 6 and reported in Table 2.

In order to analyze the stress concentrations inside the vessel wall, we report in Figure 7 the VM stresses distribution (computed with (3)) at the diastolic peak for each patient and for each stenosis degree, both for RA and SV grafts. Similarly to RRT, we observe that VM stresses are higher for the SV cases. This is confirmed by the averaged-in-space VM values computed in the same regions of interest of Figure 7 and reported in Table 3. Although VM stresses decrease for increasing stenosis degree, we observe that this trend is less pronounced than for RRT.

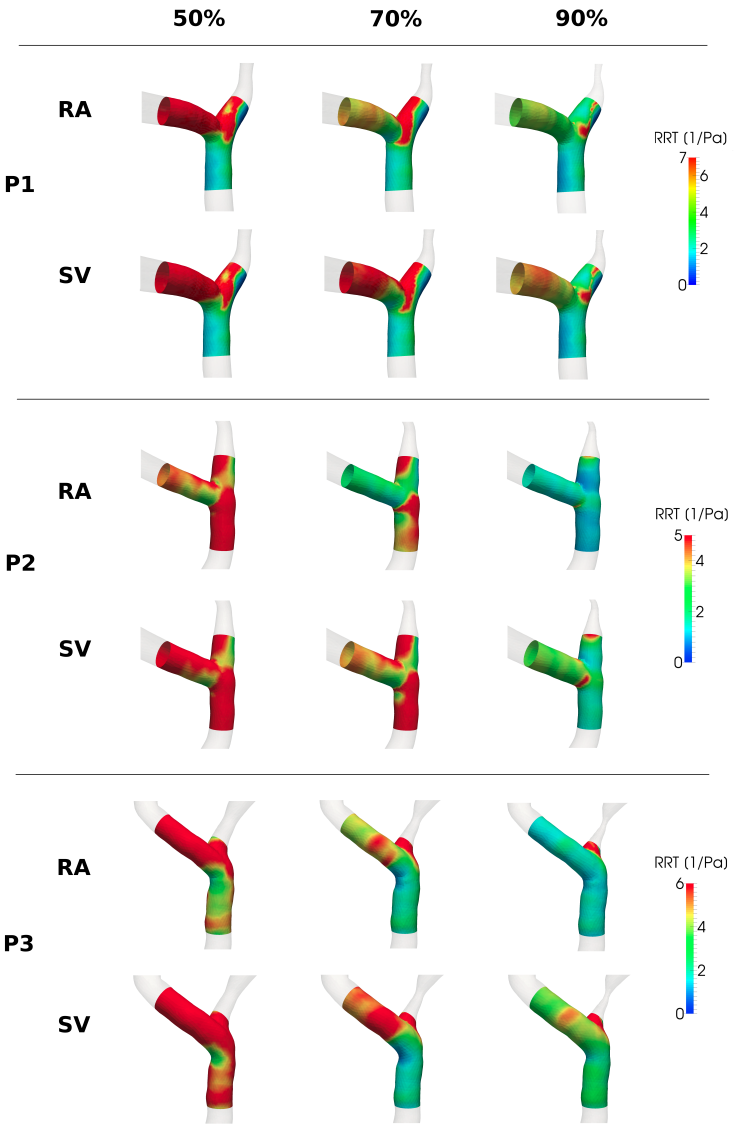

Figure 6: RRT distribution for each patient and stenosis degree, both for RA and SV grafts.

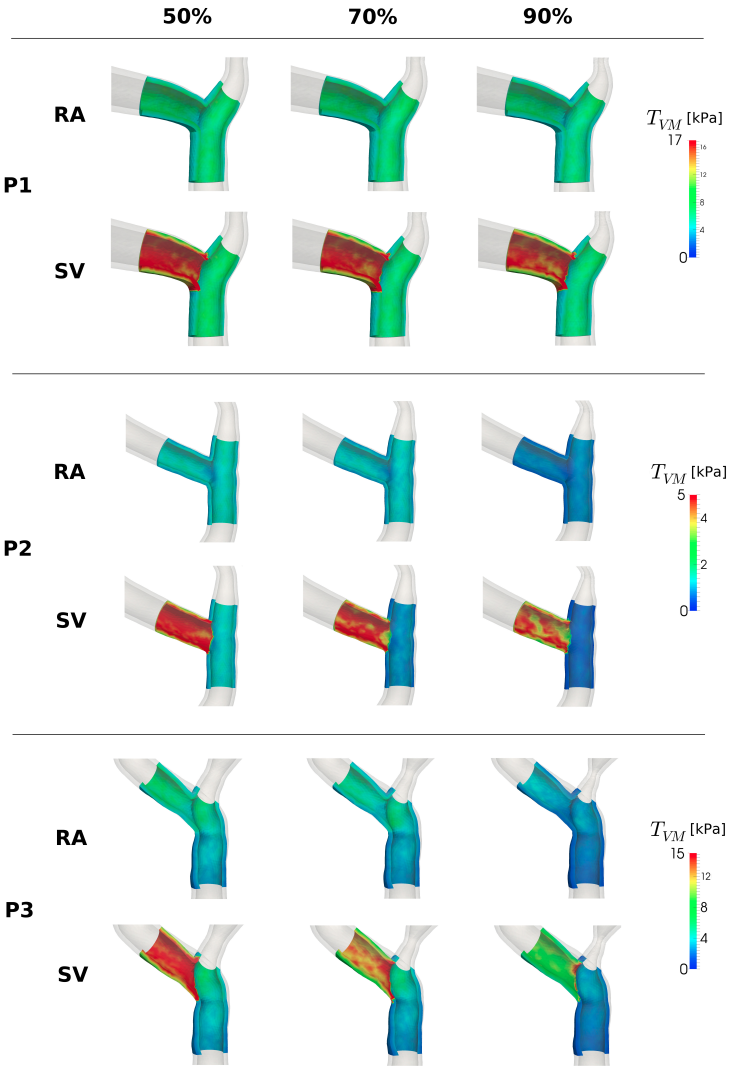

Figure 7: VM stresses distribution at the diastolic peak for each patient and stenosis degree, both for RA and SV grafts.

Table 3: Averaged-in-space VM stresses (in kPa) at the diastolic peak for each patient and stenosis degree, both for RA and SV grafts.

		50%	70%	90%
P1	RA	5.4	5.1	5.1
	SV	9.2	8.9	8.7
P2	RA	1.1	0.9	0.6
	SV	2.8	1.8	1.7
P3	RA	3.6	3.1	1.9
	SV	7.3	6.1	3.8

4 Discussion

4.1 State of the art and choice of the computational model

Most of the computational studies that have analyzed Intimal Hyperplasia formation in Coronary Artery Bypass Graft anastomoses focused on hemodynamics (see e.g. [60, 50, 51]). The first attempts to include also mechanical analyses in the vessel wall were done in [6], which performed in idealized anastomoses a structural analysis with different Young's moduli for the native arteries and the graft by prescribing a given constant-in-space internal pressure to surrogate the interaction with blood, and in [23], where the authors considered a Fluid-Structure Interaction problem in idealized geometries using a linear elastic thin shell model. More recently, other authors considered FSI studies to analize the influence of the vessel compliance on the fluid-dynamics in idealized CABG models [56, 26, 29, 21, 47]. Among these, only [47] addressed the case of multiple bypasses.

No FSI numerical simulations have been published so far in patient-specific CABG geometries. At the best of the authors' knowledge, this is the first attempt to analyze, by means of a FSI modeling, both the fluid-dynamic and wall mechanic influence on IH in patient-specific CABG geometries. Moreover, in the previous FSI studies, no comparisons between venous and arterial grafts were performed. The characterization of these two different types of grafts (by means of different dimensions and Young's modulus) and the related comparison in terms of risk of graft failure due to IH development, represent therefore another contribution of the present work.

Regarding the choice of the mechanical model for the vessel wall, we assumed a linear elastic and isotropic behavior described by Hooke's law, a well accepted hypothesis for CABG [56, 26, 21, 47], even if some authors used a non-linear finite elasticity model [29]. Although we are aware that more complex relations may be used to predict the realistic behavior of the vessel elasticity (see e.g. [24]), in this first analysis we used Hooke's law. This choice is justified by the small displacements of the coronary wall (peak of about $0.05\,mm$, that is about 3% of the diameter [26, 59]), due to the small blood velocities inside (peak of about $20\,cm/s$) and to the presence of mocardium and pericardium that surround the coronaries of interest. As for the choice of Young's modulus for the arterial and venous grafts, we observe that we used a higher value for the saphenous vein. This is justified by the fact that, even though veins have a lower stiffness than arteries at the venous pressure, they exhibit increased values as a consequence of the higher strains they are subjected under the arterial pressure [57].

Concerning blood rheology, the non-Newtonian behavior of blood should be taken into account for an accurate quantification of WSS-based indices (such as RRT) in CABGs [20], in particular for FSI simulations as highlighted in [26]. Thus, in our study we adopted the Carreau-Yasuda model, which is able to correctly describe the physiological shear-thinning behavior of blood.

We finally observe that the use of absorbing resistance boundary conditions at the fluid outlets allows avoiding the generation of spurious pressure reflections (see e.g. [43]). In fact, more sophisticated strategies for the prescription of realistic boundary conditions may be used, such as those based on lumped parameters models (see e.g. [50, 27]). However, these models need an accurate

tuning of several parameters and for this reason we prefer here to use absorbing conditions.

4.2 On the risk of graft failure due to IH development

Although the precise stimuli underlying the development of IH have not been fully defined, the abnormal proliferation of smooth muscle cells (SMC) in the intima of the vessel walls, which is at the basis of IH, is believed to be related to a combination of physical, cellular and humoral factors, see [38, 40, 34]. In fact, several studies have found convincing evidence that particular fluid-dynamic and wall mechanical conditions in the region of the anastomosis between the graft and the coronary artery may trigger a series of cellular and biological responses that can lead to IH develpment [7, 32, 48, 53, 23]. On the one hand, the presence of low and/or oscillating WSS is believed to increase the shear-regulated production of mitogens such as transforming growth factor-β (TGF-β), platelet-derived growth factor (PDGF), basic fibroblast growth factor (bFGF), and endothelin-1 (ET-1), and to attenuate the production of growth inhibitors such as Nitric Oxide (NO). On the other hand, an increase in intramural stresses upregulates intimal receptors for bFGF and stimulates SMC proliferation. As a result, SMC proliferation and consequent IH development could be analyzed by means of RRT (which is a marker of low and/or oscillating WSS) and Von Mises stresses distributions.

Previous studies showed that the presence of a non-severe LAD stenosis (i.e., less than 70%) in single LIMA bypasses results in *competitive flow* between LIMA and LAD (i.e., a dominant native coronary flow with respect to graft flow), leading to a disturbed fluid-dynamics at the anastomosis possibly related to the development of IH and subsequent graft failure (see [8, 37] for clinical studies and our previous work [20] for a computational study based on RRT quantification).

The same relationship between stenosis degree and disturbed flow at the anastomosis is observed in the case of a multiple bypass in presence of a second stenosis, see Figure 6 and Table 2. Specifically, the 50% (second) stenosis degree case results in elevated RRT values at the anastomosis for both RA and SV grafts (at least twice as much with respect to the 70% case). These results suggest that graft patency may be affected by the severity of the native coronary stenosis even in the case of composite Y-grafts, as competitive flow arising in the anastomosis related to the second stenosis may create a fluid-dynamic environment which is more prone to the development of IH. Instead, Von Mises stresses do not seem to be influenced so much by the severity of the stenosis, see Figure 7 and Table 3.

Regarding the influence of the graft choice, we notice that RRT values are higher in the SV cases independently of the degree of stenosis, with averaged-in-space values that are 12% to 71% higher than in the RA cases. In particular, for P1 the worst scenario for the SV graft is found for the 50% degree case, whereas for P2 and P3 in the 90% degree case. Our results suggest that the use of the RA graft is a better choice to avoid IH formation, since it should favour the development of an undisturbed fluid-dynamics at the anastomosis. This is supported also by our mechanical analysis in the vessel walls. Indeed, there is considerable evidence that increased wall tension leads to wall hyperplasia. In particular, clinical and in vivo observations showed that the occurrence of

anastomotic IH is caused by tissue remodeling as a response to high intramural stress concentrations brought about by the artery-graft compliance mismatch [7, 1, 52, 54]. Accordingly, it was shown that anastomotic IH may be inhibited by using a graft that does not cause increased wall stress [48]. By inspecting Figure 7 and Table 3, we observe higher VM stresses in the SV graft cases, with averaged-in-space values reaching values up to 183% higher than for the RA cases. As a result of the exposure to the arterial pressure, SV grafts feature a stiffer behavior than RA grafts, resulting in a higher compliance mismatch between the graft and the coronary artery and in higher stress concentrations in the graft.

The presence of higher VM stresses and RRT in presence of a SV graft may thus explain, at least partly, its worse long-term patency with respect to the RA grafts. Also, wall mechanics can be expected to act in concert with hemodynamics producing its effect on graft patency, since the growth factors released as a consequence of high wall stresses are likely to promote IH development more easily in the regions characterized by blood stagnation and recirculation, namely in the regions of higher RRT.

Finally, we observe that for P1 and P2 a retrograde flow occurs in the graft (both for RA and SV) for 50% and 70% stenosis degrees. This is a well-known clinical issue, since bypasses with two (or more) distal anastomoses, as in the case of composite Y-grafts, may feature dominant reverse flow that do not contribute to the coronary perfusion in the grafted territory [41].

Acknowledgments

CV was partially supported by the Italian MIUR PRIN12 project no. 201289A4LX "Modelli matematici e numerici del sistema cardiocircolatorio e loro applicazione in ambito clinico".

References

[1] W. M. Abbott, J. Megerman, J. Hasson, G. L'Italien, and D. F. Warnock. Effect of compliance mismatch on vascular graft patency. *J Vasc Surg*, 5:376–382, 1987.

[2] H. A. Al-Sabti, A. Al-Kindi, K. Al-Rasadi, Y. Banerjee, K. Al-Hashmi, and A. Al-Hinai. Saphenous vein graft vs. radial artery graft searching for the best second coronary artery bypass graft. *J Saudi Heart Assoc*, 25:247–254, 2013.

[3] T. Athanasiou, S. Saso, R. C, J. Vecht, J. Grapsa, J. Dunning, M. Lemma, and R. Casula. Radial artery versus saphenous vein conduits for coronary artery bypass surgery: forty years of competition - which conduit offers better patency? A systematic review and meta-analysis. *Eur J Cardiothorac Surg*, 40:208–220, 2011.

[4] S. Badia, F. Nobile, and C. Vergara. Fluid-structure partitioned procedures based on Robin transmission conditions. *J Comput Phys*, 227:7027–7051, 2008.

[5] N. G. Baikoussis, N. A. Papakonstantinou, and E. Apostolakis. Radial artery as graft for coronary artery bypass surgery: advantages and disadvantages for its usage focused on structural and biological characteristics. *J Cardiology*, 63:321–328, 2014.

[6] P. D. Ballik, C. Walsh, J. Butany, and M. Ojha. Compliance mismatch may promote graft-artery intimal hyperplasia by altering suture-line stresses. *J Biomech*, 31:229–237, 1998.

[7] H. S. Bassiouny, S. White, S. Glagov, E. Choi, D. P. Giddens, and C. K. Zarins. Anastomotic intimal hyperplasia: mechanical injury or flow induced. *J Vasc Surg*, 15:708–717, 1992.

[8] A. Berger, P. A. MacCarthy, U. Siebert, S. Carlier, W. Wijns, G. Heyndrickx, J. Bartunek, H. Vanermen, and B. D. Bruyne. Long-term patency of internal mammary artery bypass grafts - Relationship with preoperative severity of the native coronary artery stenosis. *Circulation*, 110:36–40, 2004.

[9] B. F. Buxton and P. A. Hayward. The art of arterial revascularization - total arterial revascularization in patients with triple vessel coronary artery disease. *Ann Cardiothorac Surg*, 2(4):543–551, 2013.

[10] P. B. Canham, H. M. Finlay, and D. R. Boughner. Contrasting structure of the saphenous vein and internal mammary artery used as coronary bypass vessels. *J Thorac Cardiac Thorac Surg*, 146:255–261, 2013.

[11] C. Cao, C. Manganas, M. Horton, P. Bannon, S. Munkholm-Larsen, S. C. Ang, and T. D. Yan. Angiographic outcomes of radial artery versus saphenous vein in coronary artery bypass surgery: a meta-analysis of randomized controlled trials. *J Thorac Cardiac Thorac Surg*, 146:255–261, 2013.

[12] A. H. Chen, T. Nakao, R. F. Brodman, M. Greenberg, R. Charney, M. Menegus, M. Johnson, R. Grose, R. Frame, E. C. Hu, H.-K. Choi, and S. Safyer. Early postoperative angiographic assessment of radial artery grafts used for coronary artery bypass grafting. *J Thorac Cardiovasc Surg*, 111(6):1208–1212, 1996.

[13] Y. I. Cho and K. R. Kensey. Effects of the non-Newtonian viscosity of blood on flows in a diseased arterial vessel. *Biorheology*, 28:241–262, 1991.

[14] S. Deb, E. A. Cohen, S. K. Singh, D. Une, A. Laupacis, and S. E. Fremes. Radial artery and saphenous vein patency more than 5 years after coronary artery bypass surgery - Results from RAPS (Radial Artery Patency Study). *J Am Coll Cardiol*, 60:28–35, 2012.

[15] J. Donea. An arbitrary Lagrangian-Eulerian finite element method for transient dynamic fluid-structure interaction. *Comput Method Appl Mech Eng*, 33:689–723, 1982.

[16] M. Fernández, J. Gerbeau, and C. Grandmont. A projection semi-implicit scheme for the coupling of an elastic structure with an incompressible fluid. *Int J Numer Meth Eng*, 69(4):794–821, 2007.

[17] T. Frauenfelder, E. Boutsianis, T. Schertler, L. Husmann, S. Leschka, D. Poulikakos, B. Marincek, and H. Alkadhi. Flow and wall shear stress in end-to-side and side-to-side anastomosis of venous coronary artery bypass grafts. *Biomed Eng Online*, 6:35, 2007.

[18] L. Gerardo Giorda, F. Nobile, and C. Vergara. Analysis and optimization of robin-robin partitioned procedures in fluid-structure interaction problems. *SIAM J Numer Anal*, 48(6):2091–2116, 2010.

[19] G. Gigante and C. Vergara. Analysis and optimization of the generalized schwarz method for elliptic problems with application to fluid-structure interaction. *Numer Math*, 131(2):369–404, 2015.

[20] B. Guerciotti, C. Vergara, S. Ippolito, A. Quarteroni, C. Antona, and R. Scrofani. Computational study of the risk of restenosis in coronary bypasses. *Biomech Model Mechanobiol*, 2016. doi:10.1007/s10237-016-0818-x.

[21] B. A. Hamedani and M. Navidbakhsh. Blood flow pattern in bending coronaries in coronary artery bypass grafts. *J Forensic Biomed*, 6(122), 2015. doi:10.4172/2090-2697.1000122.

[22] L. D. Hillis, P. K. Smith, J. L. Anderson, J. A. Bittl, C. R. Bridges, J. G. Byrne, J. E. Cigarroa, V. J. DiSesa, L. F. Hiratzka, A. M. Hutter, M. E. Jessen, E. C. Keeley, S. J. Lahey, R. A. Lange, M. J. London, M. J. Mack, M. R. Patel, J. D. Puskas, J. F. Sabik, O. Selnes, D. M. Shahian, J. C. Trost, and M. D. Winniford. ACCF/AHA guideline for coronary artery bypass graft surgery. *Circulation*, 124:652–735, 2011.

[23] M. Hofer, G. Rappitsch, K. Perktold, W. Trubel, and H. Schima. Numerical study of wall mechanics and fluid dynamics in end-to-side anastomoses and correlation to intimal hyperplasia. *J Biomech*, 29:1297–1308, 1996.

[24] G. A. Holzapfel, T. C. Gasser, and R. W. Ogden. A new constitutive framework for arterial wall mechanics and a comparative study of material models. *J Elast*, 61:1–48, 2000.

[25] T. J. R. Hughes, W. K. Liu, and T. K. Zimmermann. Lagrangian-Eulerian finite element formulation for incompressible viscous flows. *Comput Method Appl Mech Eng*, 29(3):329–349, 1981.

[26] F. Kabinejadian and D. N. Ghista. Compliant model of a coupled sequential coronary arterial bypass graft: effects of vessel wall elasticity and non-newtonian rheology on blood flow regime and hemodynamic parameters distribution. *Med Eng Phys*, 34:860–872, 2012.

[27] H. J. Kim, I. E. Vignon-Clementel, C. A. Figueroa, K. E. Jansen, and C. A. Talor. Developing computational methods for three-dimensional finite element simulations of coronary blood flow. *Finite Elem Anal Des*, 46:514–525, 2010.

[28] R. E. Klabunde. *Cardiovascular physiology concepts, 2nd Ed.* Lippincott Williams & Wilkins, 2012.

[29] E. Kouhi, Y. S. Morsi, and S. H. Masood. Haemodynamic analysis of coronary artery bypass grafting in a non-linear deformable artery and newtonian pulsatile blood flow. *Proc Inst Mech Eng H*, 222(8):1273–1287, 2008.

[30] S. Laurent, X. Gurerd, J.-J. Mourad, P. Lacolley, L. Beck, P. Boutouyrie, J.-P. Mignot, and M. Safar. Elastic modulus of the radial artery wall material is not increased in patients with essential hypertension. *Arterioscler Thromb Vasc Biol*, 14(7):1223–1231, 1994.

[31] F. Leckie and D. Bello. *Strength and stiffness of engineering systems*. Springer, 2009.

[32] S. Lee and L. R. T. Mechanical stretch and intimal hyperplasia the missing link? *Arterioscler Thromb Vasc Biol*, 30(3):459–460, 2010.

[33] S. W. Lee, L. Antiga, and D. A. Steinman. Correlations among indicators of disturbed flow at the normal carotid bifurcation. *J Biomech Eng*, 131(6):061013, 2009. doi:10.1115/1.3127252.

[34] M. S. Lemson, J. H. M. Tordoir, M. J. A. P. Daemen, and P. J. E. H. M. Kitslaar. Intimal hyperplasia in vascular grafts. *Eur J Vasc Endovasc Surg*, 19:336–350, 2000.

[35] M. S. Lemson, J. H. M. Tordoir, D. M. J. A. P, and K. P. J. E. H. M. Intimal hyperplasia in vascular grafts. *Eur J Endovasc Surg*, 19:336–350, 2000.

[36] S. Maddock, G. H. L. Tang, W. S. Aronow, and R. Malekan. *Total Arterial Revascularization in Coronary Artery Bypass Grafting Surgery*. InTech, 2013.

[37] X. Meng, Q. Fu, W. Sun, J. Yu, Y. W, and W. Bi. Competitive flow arising from varying degrees of coronary artery stenosis affects the blood flow and the production of nitric oxide and endothelin in the internal mammary artery. *Eur J Cardio-Thorac*, 43:1022–1027, 2013.

[38] A. K. Mitra, D. M. Gangahar, and D. K. Agrawal. Cellular, molecular and immunological mechanisms in the pathophysiology of vein graft intimal hyperplasia. *Immunol Cell Biol*, 84:115–124, 2006.

[39] P. Moireau, N. Xiao, M. Astorino, C. A. Figueroa, D. Chapelle, C. A. Taylor, and J.-F. Gerbeau. External tissue support and fluid-structure simulation in blood flows. *Biomech Model Mechanobiol*, 11(1-2):1–18, 2012.

[40] J. G. Motwani and E. J. Topol. Aortocoronay saphenous vein graft disease. Pathogenesis, predisposition, and prevention. *Circulation*, 97:916–931, 1998.

[41] H. Nakajima, J. Kobayashi, O. Tagusari, K. Niwaya, T. Funatsu, A. Kawamura, T. Yagihara, and S. Kitamura. Angiographic flow grading and graft arrangement of arterial conduits. *J Thorac Cardiovasc Surg*, 132(5):1023–1029, 2006.

[42] C. Narin, I. Kiris, and B. Abud. Arterial grafts in coronary artery bypass surgery. *J Cardiol Clin Res*, 4(2):1058, 2016.

[43] M. G. Nestola, E. Faggiano, C. Vergara, R. M. Lancellotti, S. Ippolito, C. Antona, S. Filippi, A. Quarteroni, and R. Scrofani. Computational comparison of aortic root stresses in presence of stentless and stented aortic valve bio-prostheses. *Comput Methods Biomech Biomed Engin*, 2016. doi:10.1080/10255842.2016.1207171.

[44] F. Nobile, M. Pozzoli, and C. Vergara. Time accurate partitioned algorithms for the solution of fluid–structure interaction problems in haemodynamics. *Comput Fluids*, 86:470–482, 2013.

[45] F. Nobile and C. Vergara. An effective fluid-structure interaction formulation for vascular dynamics by generalized Robin conditions. *SIAM J Sc Comp*, 30(2):731–763, 2008.

[46] A. A. Owida, H. Do, and Y. S. Morsi. Numerical analysis of coronary artery bypass grafts: an overview. *Comput Methods Programs Biomed*, 108:689–705, 2012.

[47] M. Pachenari and M. Alizadeh. Estimation and comparison of T graft versus conventional graft for coronary arteries. *World Applied Sciences Journal*, 10:1336–1344, 2013.

[48] F. Pomposelli, F. S. Schoen, R. Cohen, D. O'Leary, W. R. Johnson, and P. N. Madras. Conformational stress and anastomotic hyperplasia. *J Vasc Surg*, 1(4):525–535, 1984.

[49] A. Quarteroni and A. Valli. *Numerical approximation of partial differential equations*. Springer, 1994.

[50] S. Sankaran, M. E. Moghadam, A. M. Kahn, E. E. Tseng, J. M. Guccione, and A. L. Marsden. Patient-specific multiscale modeling of blood flow for coronary artery bypass graft surgery. *Ann Biomed Eng*, 40(10):2228–2242, 2012.

[51] M. Sankaranarayanan, D. N. Ghista, L. P. Chua, Y. S. Tan, and G. S. Kassab. Analysis of blood flow in an out-of-plane CABG model. *Am. J. Physiol. Heart Circ. Physiol.*, 291:H283–H295, 2242, 2006.

[52] V. S. Sottiurai, J. S. T. Yao, R. C. Batson, S. L. Sue, R. Jones, and Y. A. Nakamura. Distal anastomotic intimal hyperplasia: histopathologic character and biogenesis. *Ann Vasc Surg*, 3:26–33, 1989.

[53] S. F. C. Stewart and L. D. J. Effects of an artery/vascular graft compliance mismatch on protein transport: a numerical study. *Ann Biomed Eng*, 32(7):991–1006, 2004.

[54] W. Trubel, A. Moritz, H. Schima, F. Raderer, R. Scherer, R. Ullrich, U. Losert, and P. Polterauer. Compliance and formation of distal anastomotic intimal hyperplaisa in dacron mech tube constricted veins used as arterial bypass grafts. *ASAIO J*, 40:M273–M278, 1994.

[55] J. Vimmr, A. Jonašóvá, and O. Bublík. Numerical analysis of non-Newtonian blood flow and wall shear stress in realistic single, double and triple aorto-coronary bypasses. *Int J Numer Method Biomed Eng*, 29:1057–1081, 2013.

[56] J. Wen, G. Ding, W. Jiang, Q. Wang, and T. Zheng. Numerical simulation of compliant artery bypass grafts using fluid-structure interaction framework. *ASAIO J.*, 60(5):533–540, 2014.

[57] R. L. Wesly, R. N. Vaishnav, J. C. Fuchs, D. J. Patel, and J. C. Greenfield. Static linear and nonlinear elastic properties of normal and arterialized venous tissue in dog and man. *Circ Res*, 37:509–520, 1975.

[58] J.-H. Wi, H.-C. Joo, Y.-N. Youn, S.-W. Song, T. H. Kim, and K.-J. Yoo. Comparison of radial artery and saphenous vein composite Y grafts during off-pump coronary artery bypass. *Korean J Thorac Cardiovasc Surg*, 46:265–273, 2013.

[59] D. Zeng, E. Boutsianis, M. Ammann, K. Boomsma, S. Wildermuth, and D. Poulikakos. A study on the compliance of a right coronary artery and its impact on wall shear stress. *J Biomech Eng*, 130:1–11, 2008.

[60] J. M. Zhang, L. P. Chua, D. N. Ghista, S. C. M. Yu, and Y. S. Tan. Numerical investigation and identification of susceptible sites of atherosclerotic lesion formation in a complete coronary artery bypass model. *Med Biol Eng Comput*, 46(7):689–699, 2008.

[61] H. Zhu and M. H. Friedman. Relationship between the dynamic geometry and wall thickness of a human coronary artery. *Arterioscler Thromb Vasc Biol*, 23:2260–2265, 2003.

MOX Technical Reports, last issues

Dipartimento di Matematica
Politecnico di Milano, Via Bonardi 9 - 20133 Milano (Italy)

55/2016 Antonietti, P. F.; Facciola' C.; Russo A.; Verani M.;
Discontinuous Galerkin approximation of flows in fractured porous media on polytopic grids

54/2016 Vergara, C.; Le Van, D.; Quadrio, M.; Formaggia, L.; Domanin, M.
Large Eddy Simulations of blood dynamics in abdominal aortic aneurysms

52/2016 Paolucci, R.; Evangelista, L.; Mazzieri, I.; Schiappapietra, E.
The 3D Numerical Simulation of Near-Source Ground Motion during the Marsica Earthquake, Central Italy, 100 years later

53/2016 Antonietti, P. F.; Manzini, G.; Verani, M.
The fully nonconforming Virtual Element method for biharmonic problems

51/2016 Guzzetti, S.; Perotto, S.; Veneziani, A.
Hierarchical Model Reduction for Incompressible Flows in Cylindrical Domains: The Axisymmetric Case

49/2016 Formaggia, L.; Scotti, A.; Sottocasa, F.
ANALYSIS OF A MIMETIC FINITE DIFFERENCE APPROXIMATION OF FLOWS IN FRACTURED POROUS MEDIA

48/2016 Scardulla, S.; Pasta, S.; D'Acquisto, L.; Sciacca, S.; Agnese, V.; Vergara, C.; Quarteroni, A.; C
Shear Stress Alterations in the Celiac Trunk of Patients with Continuous-Flow Left Ventricular Assist Device by In-Silico and In-Vitro Flow Analysis

50/2016 Ambrosi, D.; Pezzuto, S.; Riccobelli, D.; Stylianopoulos, T.; Ciarletta, P.
Solid tumors are poroelastic solids with a chemo--mechanical feedback on growth

47/2016 Canuto, C.; Nochetto, R. H.; Stevenson R.; Verani, M.
On p-Robust Saturation for hp-AFEM

46/2016 Lila, E.; Aston, J.A.D.; Sangalli, L.M.
Smooth Principal Component Analysis over two-dimensional manifolds with an application to Neuroimaging